Journal of Alloys and Compounds 909 (2022) 164756

Contents lists available at ScienceDirect

Journal of Alloys and Compounds

journal homepage: www.elsevier.com/locate/jalcom

Research Article

Thermal expansion and compressibility of calcium scandate $CaSc_2O_4$

Weihong Xue[a], Xinyu Lei[a,b], Kuan Zhai[a,b], Wen Wen[c], Sheng Jiang[c], Shuangmeng Zhai[a,*]

[a] Key Laboratory of High-temperature and High-pressure Study of the Earth's Interior, Institute of Geochemistry, Chinese Academy of Sciences, Guiyang 550081, China
[b] University of Chinese Academy of Sciences, Beijing 100049, China
[c] Shanghai Synchrotron Radiation Facility, Shanghai Advanced Research Institute, Chinese Academy of Sciences, Shanghai 201210, China

ARTICLE INFO

Article history:
Received 17 January 2022
Received in revised form 21 March 2022
Accepted 23 March 2022
Available online 26 March 2022

Keywords:
$CaSc_2O_4$
In-situ X-ray diffraction
Thermal expansion
Compressibility
Heat capacity

ABSTRACT

By using in-situ synchrotron angle-dispersive X-ray diffraction measurements, the thermal expansion and compressibility of orthorhombic $CaSc_2O_4$ were investigated up to 1173 K at ambient pressure and up to 15.9 GPa at room temperature, respectively. No phase transformation was observed in this study. The thermal expansion coefficients of $CaSc_2O_4$ were determined to be $4.17(3) \times 10^{-5}$ K^{-1}, $1.60(1) \times 10^{-5}$ K^{-1}, $1.18(1) \times 10^{-5}$ K^{-1} and $1.39(1) \times 10^{-5}$ K^{-1} for the *V*, *a*-, *b*- and *c*-axis, respectively. The isothermal bulk modulus of $CaSc_2O_4$ was obtained as 153.8(50) GPa with its first pressure derivative of 6.5(9). The axial compressibility was estimated to be 123(3), 177(4) and 242(11) GPa for the *a*-, *b*- and *c*-axis, respectively. Both the thermal expansion and compressibility of $CaSc_2O_4$ show axial anisotropy. The heat capacities (C_v and C_p) of $CaSc_2O_4$ was estimated by using a Kieffer model with Raman spectroscopy data and present experimental results. The standard entropy (S^0_{298}) and Debye temperature (θ_D) of $CaSc_2O_4$ were also calculated.

1. Introduction

Oxide compounds with the chemical formula of AB_2O_4 (A = divalent cation, B = trivalent cation) have been well investigated due to their various structural, physical and chemical properties and extensive applications. Calcium scandium oxide (also referred to as calcium scandate), $CaSc_2O_4$, belongs to this family, and has been widely adopted as a host to synthesize fluorescent materials with different kinds of dopants [1–15]. This phase of $CaSc_2O_4$ can be obtained through high-temperature calcination at ambient pressure. The structure of $CaSc_2O_4$ was described and refined in the orthorhombic with space group of *Pnam*, containing four formula units for a total of 28 atoms [16–18]. In the crystal structure (Fig. 1), all of the constituent atoms occupy 4c sites according to the Wyckoff notation. The Ca atoms are coordinated by eight oxygen atoms, and the Sc atoms occupy two different kinds of positions where each is coordinated by six oxygen atoms. The orthorhombic structure includes a double octahedral Sc_2O_4-framework and Ca atoms residing within the framework with the bicapped trigonal prismatic site.

To improve the application of materials, it is fundamental to know their physical and chemical properties. Although $CaSc_2O_4$ is widely used to obtain luminescent matter, little information about the physical and chemical properties of $CaSc_2O_4$ is available. In a previous study, the chemical bond characteristics, thermal expansion property and compressibility of $CaSc_2O_4$ were theoretically studied [19]. However, no information on these physical properties was experimentally reported. In this paper, we investigated the physical properties of the thermal expansion and compressibility of $CaSc_2O_4$ by in-situ synchrotron radiation X-ray diffraction measurements under various temperatures and high pressures. Additionally, the thermodynamic properties including heat capacity, entropy and Debye temperature, were estimated by using the Kieffer vibrational model.

2. Materials and methods

High-purity $CaSc_2O_4$ was prepared by a solid-state reaction from $CaCO_3$ and Sc_2O_3. Reagent-grade $CaCO_3$ and Sc_2O_3 powders were mixed in the proportion corresponding to the $CaSc_2O_4$ stoichiometry, and the mixture was ground sufficiently and pressed into pellets with a diameter of 8 mm under uniaxial pressure of 15 MPa. The pellets were sintered at 1673 K in a furnace for 72 h, during which the sample was cooled, ground, and heated three times. The sintered product was confirmed by a powder X-ray diffractometer as a single $CaSc_2O_4$ phase.

* Corresponding author.
E-mail address: zhaishuangmeng@mail.gyig.ac.cn (S. Zhai).

https://doi.org/10.1016/j.jallcom.2022.164756
0925-8388/

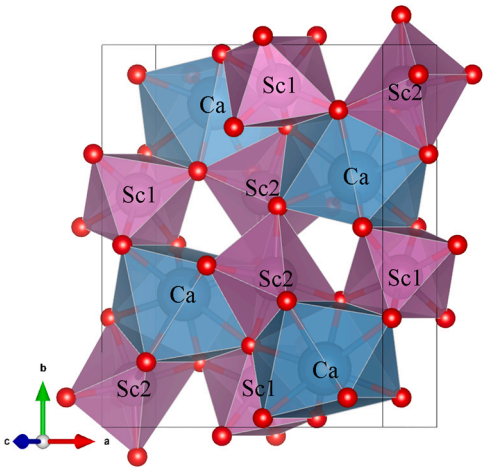

Fig. 1. The crystal structure of $CaSc_2O_4$.

In-situ angle-dispersive X-ray diffraction measurements at various temperatures were carried out at BL14B1 beamline of Shanghai Synchrotron Radiation Facility (SSRF), China. The description of this beamline was previously reported [20]. The experimental procedure was the same as those in previous studies [21,22]. The powdered $CaSc_2O_4$ sample was put into a fused quartz capillary and set at the center of a custom-made furnace, which could generate the target temperature with a rate of 30 K/min. The temperature was automatically controlled by a program and monitored by a K-type thermocouple with an accuracy of approximately ± 1 K. The wavelength of the in-situ monochromatic X-ray was 0.6887 Å, which was calibrated with a NIST LaB_6 standard (660b). The beam size is about 200 μm (height) × 180 μm (width). Before each collection of the XRD pattern, the desired temperature was held for 5–10 min for thermal equilibrium. Each XRD pattern was measured in a 2θ range of 10°–40° with a step of 0.01° up to the temperature of 1173 K. The lattice parameters of the sample at various temperatures were obtained by refinements of XRD patterns using GSAS software [23,24].

In-situ angle dispersive X-ray diffraction experiments at different pressures were done at BL15U1 beamline of SSRF. The details of this beamline were previously described [25]. The experimental procedure was similar to previous studies [26,27]. A monochromatic X-ray with a wavelength of 0.6199 Å was used and the beam spot on the sample was about 5 μm in diameter. A symmetry-type diamond anvil cell (DAC) was adopted. The culets of the diamond anvils are 500 μm in diameter. A T301 stainless steel disk with an initial thickness of 260 μm was pre-indented to about 50 μm in thickness and used as a gasket. A hole as the sample chamber with a diameter of 200 μm was drilled. The $CaSc_2O_4$ sample, pressure scale of ruby (Cr^{3+} doped α-Al_2O_3) microspheres and pressure medium of silicone oil, were loaded into the chamber. The experimental pressures were determined by the ruby fluorescence method [28]. Collection time for each pattern was 120 s. All collected images were integrated using the DIOPTAS program [29] to obtain conventional one-dimensional diffraction patterns, which were analyzed by the LeBail method implemented in GSAS+EXPGUI software [23,24] to obtain the cell parameters.

3. Results and discussion

3.1. Thermal expansion

High-temperature X-ray diffraction patterns were collected up to 1173 K at ambient pressure. Fig. 2 shows typical X-ray diffraction patterns obtained in this study. All the diffraction peaks can be assigned to orthorhombic $CaSc_2O_4$. The X-ray diffraction pattern of

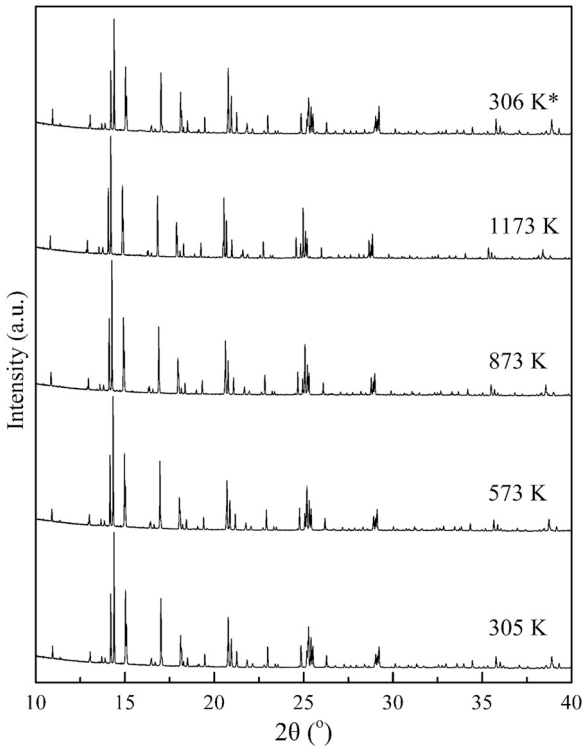

Fig. 2. Typical X-ray diffraction patterns of $CaSc_2O_4$ at different temperatures and ambient pressure.

$CaSc_2O_4$ under ambient conditions gives unit-cell parameters of a_0 = 9.4803(1) Å, b_0 = 11.1337(1) Å, c_0 = 3.1475(1) Å and V_0 = 332.23(1) $Å^3$, which are consistent with previous studies [16–18]. With increasing temperature, the X-ray diffraction peaks shift to the lower 2θ region, and no phase transition occurs. A refined plot of X-ray diffraction pattern collected at a temperature of 305 K is shown in Fig. 3. The obtained *V-T* data of $CaSc_2O_4$ at different temperatures are listed in Table 1. The variations in the lattice parameters (*a, b, c, V*) of $CaSc_2O_4$ are displayed in Fig. 4.

The thermal expansion coefficient $\alpha_v = 1/V\,(\partial V/\partial T)_P$ can be used to express the fluctuation of lattice parameters as a function of temperature. Provided the thermal expansion coefficient α_v does not vary with temperature, integration gives the following formula [30]:

$$\ln\,(V/V_0) = \alpha_v\,(T - T_0) \quad (1)$$

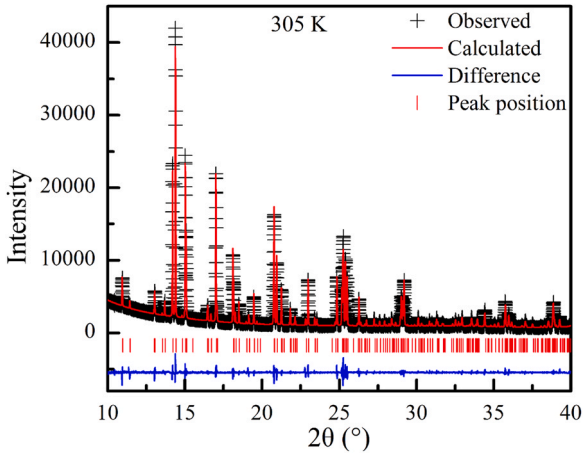

Fig. 3. Refined X-ray diffraction pattern of $CaSc_2O_4$ obtained at 305 K. Observed (black crosses), calculated (red line) and difference (bottom blue curve) powder XRD pattern determined by Rietveld analysis.

Table 1
Lattice parameters of $CaSc_2O_4$ at various temperatures.

T (K)	a (Å)	b (Å)	c (Å)	V (Å^3)
305	9.4803(1)	11.1337(1)	3.1475(1)	332.23(1)
373	9.4867(1)	11.1372(1)	3.1491(1)	332.72(1)
473	9.5070(1)	11.1563(1)	3.1549(1)	334.62(1)
573	9.5219(1)	11.1684(1)	3.1592(1)	335.96(1)
673	9.5373(1)	11.1816(1)	3.1637(1)	337.38(1)
773	9.5517(1)	11.1942(1)	3.1678(1)	338.71(1)
873	9.5678(1)	11.2089(1)	3.1726(1)	340.24(1)
973	9.5828(1)	11.2215(1)	3.1770(1)	341.63(1)
1073	9.5973(1)	11.2354(1)	3.1814(1)	343.05(1)
1173	9.6122(1)	11.2492(1)	3.1860(1)	344.50(1)

Standard deviations are in parentheses.

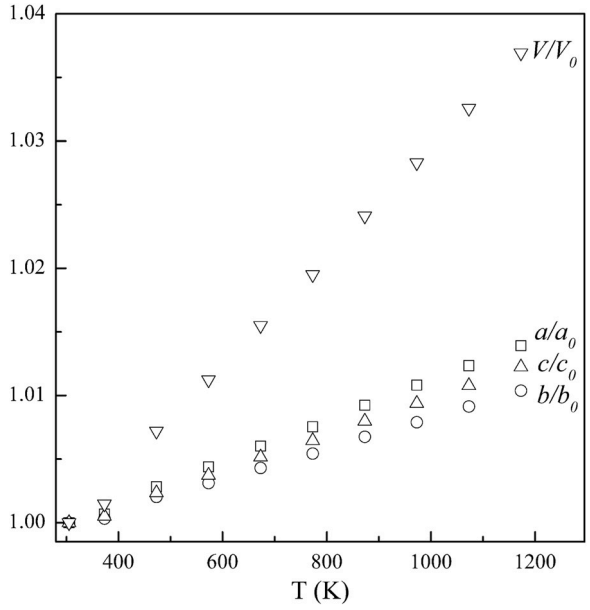

Fig. 4. Variations in lattice parameters with temperature for $CaSc_2O_4$.

In the same way, the axial thermal expansion coefficients along the *a*-, *b*- and *c*-axis can be obtained by the following expressions:

$$\ln (a/a_0) = \alpha_a (T - T_0) \quad (2)$$

$$\ln (b/b_0) = \alpha_b (T - T_0) \quad (3)$$

$$\ln (c/c_0) = \alpha_c (T - T_0) \quad (4)$$

Using the refined *V-T* data listed in Table 1 and the above formulas, the thermal expansion coefficients of $CaSc_2O_4$ are obtained as $4.17(3) \times 10^{-5}$ K^{-1}, $1.60(1) \times 10^{-5}$ K^{-1}, $1.18(1) \times 10^{-5}$ K^{-1} and $1.39(1) \times 10^{-5}$ K^{-1} for volume, *a*-, *b*- and *c*-axis, respectively. In a previous study, the linear thermal expansion coefficient (α_L) of $CaSc_2O_4$ was theoretically predicted as 1.17×10^{-6} K^{-1} [19]. Indeed, α_L is one-third of α_v [31]. However, the deduced linear thermal expansion coefficient is 1.39×10^{-6} K^{-1} in this study, which is larger than the theoretical calculation.

Obviously, axial thermal expansion anisotropy exists in $CaSc_2O_4$ since the *a*-axis shows a larger thermal expansion coefficient than those of the *b*- and *c*-axis. This is reasonable since the atomic arrangement along the *a*-axis is looser than those along the *b*- and *c*-axis [18]. The anisotropic axial thermal expansion characteristic of $CaSc_2O_4$ is similar to that of β-$CaCr_2O_4$ [22], and a thermal expansive relationship of $\alpha_v = \alpha_a + \alpha_b + \alpha_c$ also stands within $CaSc_2O_4$. Compared with our previous study of β-$CaCr_2O_4$ [22], $CaSc_2O_4$ shows relatively larger thermal expansion coefficients. In fact, in the crystal structure of $CaSc_2O_4$ [18], eight-coordinated Ca^{2+} cations yield an average Ca-O bond length of 2.5127 Å, and two different kinds of six-coordinated Sc^{3+} cations give average Sc-O bond lengths of 2.1206 Å and 2.1226 Å. These bond lengths are larger than the corresponding values of β-$CaCr_2O_4$. It is known that a larger bond length means a weaker bond force, which causes the thermal expansion of $CaSc_2O_4$ to be larger than that of β-$CaCr_2O_4$. The bond expansion can be estimated by the following empirical relation [32]:

$$<\alpha>(10^{-6}\ K^{-1}) = 32{\cdot}9 \times (3/4 - z/\rho) \quad (5)$$

where z is the cation charge and ρ is the coordination number. The expression gives bond expansion of 16.45×10^{-6} K^{-1} for ^{VIII}Ca-O and 8.225×10^{-6} K^{-1} for ^{VI}Sc-O. Obviously, Ca-O bond expansion dominates the expansion of $CaSc_2O_4$.

Due to its high thermal expansion coefficient, $CaSc_2O_4$ might be regarded as a potential thermal barrier coating (TBC). More investigations are needed to uncover if it is with high stability, high chemical resistance, low sintering rate and high fracture toughness, which are requirements for TBC materials.

3.2. Compressibility

High-pressure X-ray diffraction patterns were collected up to 15.9 GPa at ambient temperature. Fig. 5 shows typical X-ray diffraction patterns at different pressures obtained in this study. All the diffraction peaks can be assigned to $CaSc_2O_4$. With increasing pressure, the X-ray diffraction peaks shift to a higher 2θ region, and no phase transformation happens. A refined plot of X-ray diffraction pattern collected at a pressure of 4.1 GPa is illustrated in Fig. 6. The refined unit-cell parameters of $CaSc_2O_4$ at different pressures are listed in Table 2. In order to obtain the bulk modulus, the refined *P-V* values were fitted by using the following third-order Birch-Murnaghan equation of state [33]:

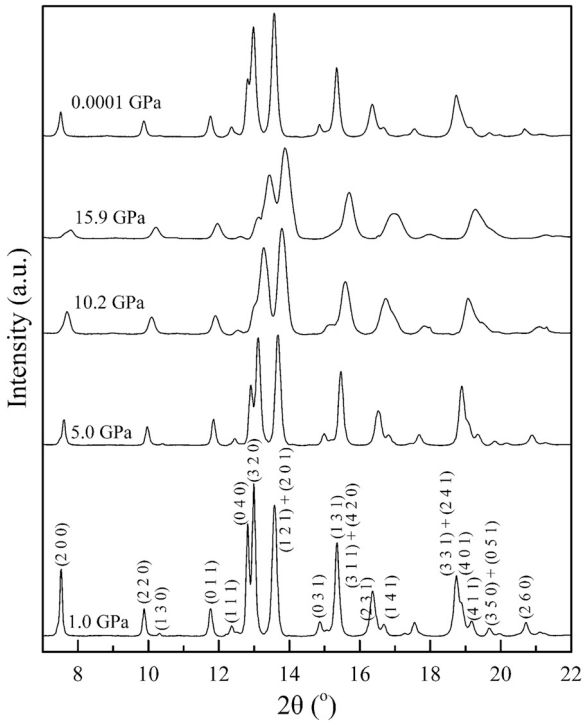

Fig. 5. Representative X-ray diffraction patterns of $CaSc_2O_4$ at high pressures and room temperature.

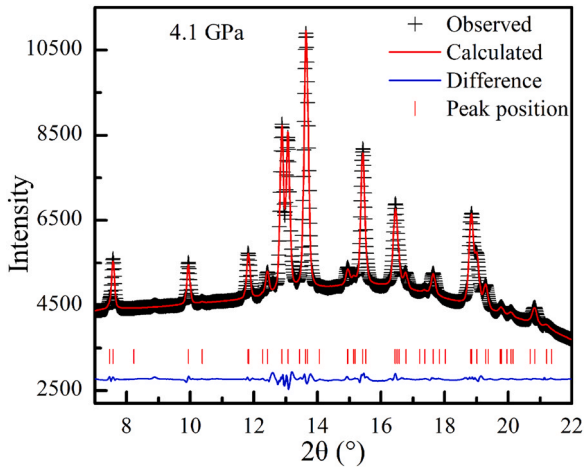

Fig. 6. Refined X-ray diffraction pattern of $CaSc_2O_4$ obtained at 4.1 GPa. Observed (black crosses), calculated (red line) and difference (bottom blue curve) powder XRD pattern determined by Rietveld analysis.

Table 2
Unit-cell parameters of $CaSc_2O_4$ at different pressures.

P (GPa)	*a* (Å)	*b* (Å)	*c* (Å)	*V* (Å^3)
0.00001[a]	9.4796(8)	11.1327(9)	3.1470(3)	332.11(6)
1.0	9.4485(2)	11.1048(3)	3.1389(1)	329.34(1)
2.3	9.4185(7)	11.0770(8)	3.1312(2)	326.67(7)
3.1	9.3990(5)	11.0642(5)	3.1273(1)	325.21(3)
4.1	9.3845(17)	11.0511(20)	3.1243(6)	324.02(17)
5.0	9.3709(4)	11.0399(5)	3.1193(1)	322.70(3)
6.4	9.3365(8)	11.0108(8)	3.1131(2)	320.03(7)
7.4	9.3120(5)	10.9956(5)	3.1075(1)	318.18(4)
8.6	9.3029(13)	10.9824(13)	3.1030(4)	317.03(12)
9.4	9.2832(22)	10.9630(24)	3.1016(7)	315.65(21)
10.2	9.2631(24)	10.9438(27)	3.0991(8)	314.16(23)
11.4	9.2357(17)	10.9131(19)	3.0967(5)	312.12(16)
12.4	9.2137(16)	10.8969(16)	3.0948(5)	310.72(14)
13.3	9.1940(18)	10.8883(19)	3.0921(6)	309.54(17)
14.5	9.1801(39)	10.8697(45)	3.0867(13)	308.00(39)
15.9	9.1505(11)	10.8564(13)	3.0858(3)	306.55(9)

Standard deviations are in parentheses.
[a] The XRD pattern at 0.0001 GPa was collected after full decompression.

$$P = \frac{3K_0}{2}\left[\left(\frac{V_0}{V}\right)^{7/3} - \left(\frac{V_0}{V}\right)^{5/3}\right]\left\{1 + \frac{3}{4}(K_0' - 4)\left[\left(\frac{V_0}{V}\right)^{2/3} - 1\right]\right\} \quad (6)$$

where P, K_0, V_0, V and K'_0 are pressure, isothermal bulk modulus, zero-pressure volume, high-pressure volume and first pressure derivative of the isothermal bulk modulus, respectively.

Using the *EosFit* program [34], a least-squares fitting yields V_0 = 331.95(11) Å^3, K_0 = 153.8 ± 5.0 GPa, and K_0' = 6.5 ± 0.9. When K_0' is fixed at 4, the fitting gives K_0 = 166.7 ± 1.9 GPa. The volume variation of $CaSc_2O_4$ as a function of pressure and the compression curve calculated by the fitted parameters are illustrated in Fig. 7. A theoretical study was carried out by using the chemical bond theory of dielectric description and yielded a bulk modulus of 121.4 GPa for $CaSc_2O_4$ [19]. Another bulk modulus of 145 GPa for $CaSc_2O_4$ was predicted by the Materials Project using the generalized gradient approximation (GGA) [35]. Generally, GGA underestimates the bulk modulus. Therefore, it is reasonable that the isothermal bulk modulus of $CaSc_2O_4$ deduced from our experimental results is larger than the theoretical calculations. Compared with isostructural β-$CaCr_2O_4$, $CaSc_2O_4$ shows a smaller isothermal bulk modulus, i.e., more compressible. Meanwhile, the empirical relationship $K_0 \times V_0$ = constant [36] for the same crystal structure is valid for $CaSc_2O_4$ and β-$CaCr_2O_4$.

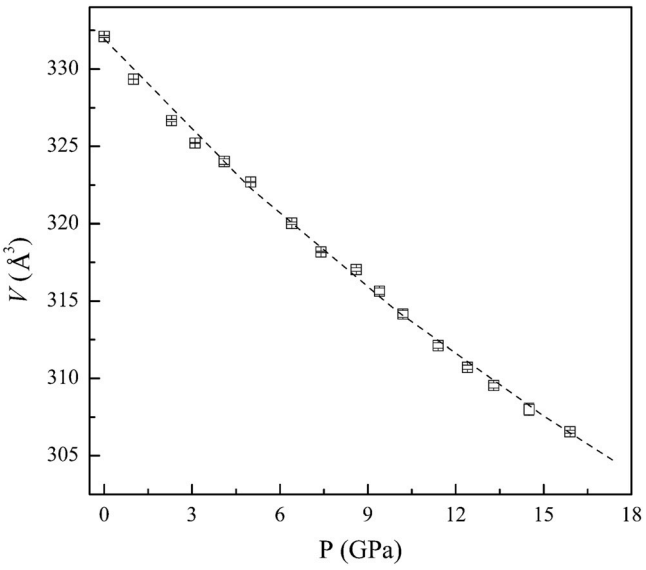

Fig. 7. *P-V* data of $CaSc_2O_4$ at high pressures and room temperature. The dash curve represents the third-order Birch-Murnaghan equation of state fitted with K_0 of 153.8 GPa and K_0' of 6.5. The uncertainties of pressure and volume are within symbols.

As mentioned above, a larger bond length means a weaker bond force and easier compression. The bond compression can be estimated by the following empirical relation [32]:

$$<\beta>(10^{-6}\ \text{kbar}^{-1}) = 37{\cdot}0 \times (d_0{}^3/z) \quad (7)$$

where d_0 is the mean polyhedral metal-oxygen distance under ambient conditions, and z is the cation charge. The expression yields bond compression of 293.5×10^{-5} GPa^{-1} for ^{VIII}Ca-O and 117.8×10^{-5} GPa^{-1} for ^{VI}Sc-O. Obviously, Ca-O bond compression is dominant to the bulk compressibility of $CaSc_2O_4$.

In order to estimate and compare the axial compressibility of $CaSc_2O_4$, a second-order Birch-Murnaghan equation of state was used to fit the values of a^3, b^3 and c^3 at different pressures. The fitting axial moduli are Ka_0 = 123(3) GPa, Kb_0 = 177(4) GPa and Kc_0 = 242(11) GPa for the *a*-, *b*- and *c*-axis, respectively. Clearly, $CaSc_2O_4$ shows axial elastic anisotropy along the *a*-, *b*- and *c*-axis since the *a*-axis is more compressible than the *b*- and *c*-axis. Similarly, the axial elastic anisotropy might be related to the structure of $CaSc_2O_4$ and polyhedral evolution under high pressures.

3.3. Heat capacity and entropy

The specific heat capacity (C_p) of $CaSc_2O_4$ has been experimental measured by using both single crystalline and powder sample [37,38]. However, the results are inconsistent. It is known that heat capacity can be calculated by the Kieffer vibrational model [39–41]. Based on the crystal structure, group factor analysis gives 84 vibrational modes including three acoustic modes and eighty-one optic modes for $CaSc_2O_4$ [42]. There is no information about the acoustic velocities of $CaSc_2O_4$, but the compressional velocity (V_p) can be calculated from the following Birch empirical relationship [43]:

$$V_p = -1{\cdot}87 - 0.7 \times (m - 21) + 3{\cdot}05\ \rho \quad (8)$$

where m is the mean atomic weight and ρ is the density in g/cm^3. The shear velocity (V_s) is calculated by the equation:

$$Vs = \frac{\sqrt{3}}{2}\left(V_p^2 - \frac{Ks}{\rho}\right)^{1/2} \quad (9)$$

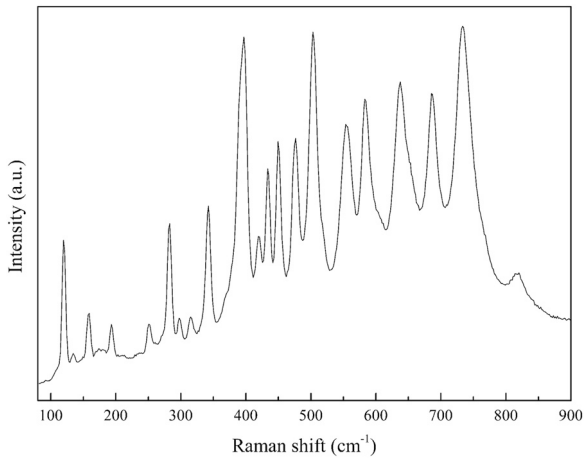

Fig. 8. Raman spectrum of $CaSc_2O_4$ at room temperature and 1 atm.

where K_S is adiabatic bulk modulus and its better approximation for most materials is $K_S = 1.01\ K_T$, where K_T is the isothermal bulk modulus as 153.8 GPa for $CaSc_2O_4$ obtained in this study. According to the method described by Kieffer [39], the directionally averaged acoustic velocities were estimated. Raman spectrum of $CaSc_2O_4$, as shown in Fig. 8, was used for modeling the vibrational density of states of optic modes in this study. Similar to our previous study of β-$CaCr_2O_4$ [22], an optic continuum model in the Raman shift range of 50–900 cm^{-1} was adopted for calculation. The isochoric heat capacity C_v was obtained from Kieffer modeling. Then the isobaric heat capacity (C_p) was calculated by the following formula:

$$C_p = C_v + \alpha_v^2\ K_T\ V_T\ T \tag{10}$$

where α_v, K_T and V_T are the thermal expansion coefficient, isothermal bulk modulus and volume, respectively, at ambient pressure and T K. The isothermal bulk modulus at ambient temperature is obtained as 153.8 GPa in this study. But the temperature derivative of K_T is not available. It was reported as - 0.03 GPa/K for orthorhombic MgAl2O4 [44], which is adopted in this study for better approximation. V_T at T K is determined using an expression of:

$$V_T = V_{298} exp \int_{298}^{T} \alpha_v\ dT \tag{11}$$

where V_{298} refers to the volume of $CaSc_2O_4$ at ambient temperature and pressure.

The estimated heat capacities (C_v and C_p) are displayed in Fig. 9. Meanwhile, the limiting C_v value can be predicted by the Dulong-Petit law ($C_{vD\text{-}P}$):

$$C_{vD\text{-}P} = 3nR \tag{12}$$

where n and R are the number of atoms in the molecule and the gas constant, respectively. Therefore, $C_{vD\text{-}P}$ is obtained as 174.5 J mol^{-1} K^{-1} for $CaSc_2O_4$, shown as a horizontal dash line in Fig. 9. Clearly, the calculated C_v curve is close to the $C_{vD\text{-}P}$ at high temperature, which means the calculation is reasonable in this study. Compared with the specific heat capacity (C_p) obtained in previous experimental differential scanning calorimetric measurements [37,38], Kieffer model gives larger values of C_p for $CaSc_2O_4$, as shown in Fig. 9.

Additionally, the calculated C_p can be used to estimate the vibrational entropy at T K according to the following formula:

$$S_T^0 = \int_0^T \frac{C_p}{T}\ dT \tag{13}$$

The vibrational entropy at 298 K (S_{298}^0) is estimated to be 117 J mol^{-1} K^{-1}, which is smaller than that of β-$CaCr_2O_4$ [22].

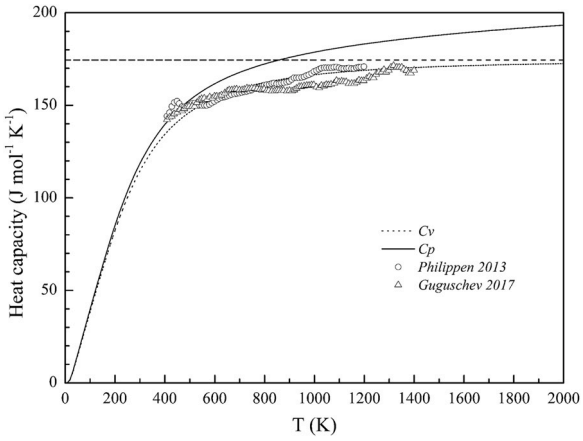

Fig. 9. Heat capacities of $CaSc_2O_4$. Solid and dashed curves show C_p and C_v given by Kieffer vibrational model. Horizontal dash line represents the Dulong-Petit limiting $C_{vD\text{-}P}$ value. Open circles and triangles are the measured C_p of $CaSc_2O_4$ in previous studies [37,38].

The Debye temperature (θ_D) is one of the most important thermodynamic parameters since it is the temperature of a crystal's highest normal mode of vibration. The Debye temperature is related to the elastic properties with the thermodynamic properties such as phonons, thermal conductivity, thermal expansion, specific heat, and lattice enthalpy [45]. The Debye temperature θ_D of $CaSc_2O_4$ can be estimated from the averaged sound velocity in the following equation [46]:

$$\theta_D = \frac{h}{k_B}\left[\frac{3n}{4\pi}\ \frac{N_A\rho}{M}\right]^{1/3} V_m, \tag{14}$$

where h, k_B, n, N_A, ρ and M represent Planck's constant, Boltzmann's constant, the number of atoms per chemical formula, Avogadro's number, density and molecular weight, respectively, and V_m is the averaged sound velocity calculated from compressional velocity V_p and shear velocity V_s with the equation:

$$V_m = \left(\frac{1}{3}\left[\frac{1}{V_p^3} + \frac{2}{V_s^3}\right]\right)^{-1/3}. \tag{15}$$

The estimated Debye temperature θ_D of $CaSc_2O_4$ is 891 K, which is higher than that of β-$CaCr_2O_4$ [22].

4. Conclusion

In this study, we investigated the physical properties of the thermal expansion and compressibility of orthorhombic $CaSc_2O_4$ by in-situ synchrotron X-ray diffraction measurements in the temperature range of 305–1173 K at ambient pressure and under pressures up to 15.9 GPa at room temperature, respectively. No temperature-induced or pressure-induced phase transformation was observed in the present study. The thermal expansion coefficient of $CaSc_2O_4$ was determined to be $4.17(3) \times 10^{-5}$ K^{-1}. The isothermal bulk modulus of $CaSc_2O_4$ was obtained as 153.8(50) GPa with its first pressure derivative of 6.5(9). Axial anisotropy exists in both thermal expansion and compressibility. The thermodynamic parameters including heat capacity, standard entropy (S_{298}^0) and Debye temperature (θ_D) of $CaSc_2O_4$ were also estimated by adopting the Kieffer vibrational model with Raman spectrum and present experimental results.

Founding sources

This work was financially supported by the National Natural Science Foundation of China (Grant Nos. 41872045, U1532126) and Chinese Academy of Sciences (Grant No. 132852KYSB20200011).

CRediT authorship contribution statement

W. Xue: Synthesis and Identification of sample, X-ray studies, Writing – original draft. **X. Lei:** Data processing. **K. Zhai:** Data processing. **W. Wen:** Methodology. **S. Jiang:** Methodology. **S. Zhai:** Conceptualization, Reviewing and Editing.

Declaration of Competing Interest

The authors declare that they have no known competing financial interests or personal relationships that could have appeared to influence the work reported in this paper.

Acknowledgements

The in-situ synchrotron X-ray diffraction measurements were carried out at the BL14B1 and BL15U1 beamlines of SSRF (Proposal Nos. 2020-SSRF-PT-013605, 2020-SSRF-PT-013770).

References

[1] M.N. Baranov, E.F. Kustov, V.P. Petrov, Crystal field spectra of Nd^{3+} ions in $SrAl_{12}O_{19}$ and $CaSc_2O_4$, Phys. Status Solid A 21 (1974) K123–K125, https://doi.org/10.1002/pssa.2210210262

[2] K.S. Bagdasarov, A.A. Kaminskii, A.M. Kevorkov, A.M. Prokhorov, Investigation of the stimulated radiation emitted by Nd^{3+} ions in $CaSc_2O_4$ crystals, Sov. J. Quantum Electron. 4 (1975) 927–928.

[3] R. Gaume, B. Viana, J. Derouet, D. Vivien, Spectroscopic properties of Yb-doped scandium based compounds Yb:$CaSc_2O_4$, Yb:$SrSc_2O_4$ and Yb:Sc_2SiO_5, Opt. Mater. 22 (2003) 107–115, https://doi.org/10.1016/S0925-3467(02)00354-3

[4] Y. Shimomura, T. Kurushima, N. Kijima, Photoluminescence and crystal structure of green-emitting phosphor $CaSc_2O_4$: Ce^{3+}, J. Electrochem. Soc. 154 (2007) J234–J238, https://doi.org/10.1149/1.2741172

[5] Z. Hao, J. Zhang, X. Zhang, S. Lu, X. Wang, Blue-green-emitting phosphor $CaSc_2O_4$: Tb^{3+}: tunable luminescence manipulated by cross-relaxation, J. Electrochem. Soc. 156 (2009) H193, https://doi.org/10.1149/1.3060382

[6] J. Meng, F. Zhang, W. Peng, W. Wan, Q. Xiao, Q. Chen, L. Cao, Z. Wang, Fluorescence properties of novel near-infrared phosphor $CaSc_2O_4$:Ce^{3+}, Nd^{3+}, J. Alloy. Compd. 508 (2010) 222–225, https://doi.org/10.1016/j.jallcom.2010.08.064

[7] W. Peng, S. Zou, G. Liu, Q. Xiao, R. Zhang, L. Xie, L. Cao, J. Meng, Y. Liu, Combustion synthesis of $CaSc_2O_4$:Ce^{3+} nano-phosphors in a closed system, J. Alloy. Compd. 509 (2011) 6673–6676, https://doi.org/10.1016/j.jallcom.2011.03.135

[8] J. Philippen, C. Guguschev, R. Bertram, D. Klimm, Laser-heated pedestal growth of cerium doped calcium scandate crystal fibers, J. Cryst. Growth 363 (2013) 270–276, https://doi.org/10.1016/j.jcrysgro.2012.11.013

[9] S. Georgescu, A. Stefan, A.M. Voiculescu, O. Toma, C. Matei, R. Birjega, Peculiarities of the Ho3+→ Yb3+ energy transfer in CaSc2O4:Ho:Yb, J. Lumin. 154 (2014) 142–147, https://doi.org/10.1016/j.jlumin.2014.04.021

[10] J. Li, J. Zhang, Z. Hao, L. Chen, X. Zhang, Y. Luo, ntense upconversion luminescence of $CaSc_2O_4$:Ho^{3+}/Yb^{3+} from large absorption cross section and energy-transfer rate of Yb^{3+}, ChemPhysChem 16 I,, 2015, pp. 1366–1369, https://doi.org/10.1002/cphc.201500011

[11] L. Feng, Z. Hao, Y. Luo, X. Zhang, L. Zhang, G. Pan, H. Wu, J. Zhang, Observation and photoluminescence properties of two Er^{3+} centers in $CaSc_2O_4$: Er^{3+}, Yb^{3+} upconverting phosphor, J. Alloy. Compd. 708 (2017) 827–833, https://doi.org/10.1016/j.jallcom.2017.03.088

[12] S.K. Sharma, M. Bettinelli, M. Karlsson, Green persistent luminescence excitable by multiple wavelengths in the $CaSc_2O_4$:Ce^{3+} phosphor co-doped with Mg^{2+}, J. Lumin. 196 (2018) 437–441, https://doi.org/10.1016/j.jlumin.2017.12.047

[13] F. Li, J. Li, Y. Wang, Y. Huang, Y. Peng, L. Chen, Impact of organic additives on synthesis and upconversion luminescence properties in Ln^{3+}, Yb^{3+} (Ln^{3+} = Er^{3+}/Tm^{3+}/Ho^{3+}) doped $CaSc_2O_4$ nanocrystals via hydrothermal method, Opt. Mater. 96 (2019) 109293, https://doi.org/10.1016/j.optmat.2019.109293

[14] X. He, X. Wang, Z. Zhang, R. Zuo, L. Wang, Enhanced red and near-infrared upconversion luminescence properties in $CaSc_2O_4$ microcrystals, Chem. Phys. Lett. 749 (2020) 137425, https://doi.org/10.1016/j.cplett.2020.137425

[15] A. Enachi, O. Toma, S. Georgescu, Luminescent Er^{3+} centers in $CaSc_2O_4$: Er^{3+}: Yb^{3+} upconversion phosphor, J. Lumin 231 (2021) 117816, https://doi.org/10.1016/j.jlumin.2020.117816

[16] J.R. Carter, R.S. Feigelson, Preparation and crystallographic properties of $A^{2+}B_2^{3+}O_4$ type calcium and strontium scandates, J. Am. Ceram. Soc. 47 (1964) 141–144, https://doi.org/10.1111/j.1151-2916.1964.tb14373.x

[17] H. Müller-Buschbaum, H.G. Schnering, Über Oxoscandate. I. Zur Kenntnis des $CaSc_2O_4$, Z. Anorg. Allg. Chem. 336 (1965) 295–305.

[18] R. Horyn, K. Lukaszew, Refinement of crystal structure of $CaSc_2O_4$, Bull. Acad. Pol. Sci. Chim. 14 (1966) 499–504.

[19] H. Li, S. Zhang, S. Zhou, X. Cao, Chemical bond characteristics, thermal expansion property and compressibility of AR_2O_4 (A= Ca, Sr, Ba; R= rare earths), Mater. Chem. Phys. 114 (2009) 451–455, https://doi.org/10.1016/j.matchemphys.2008.09.066

[20] T. Yang, W. Wen, G. Yin, X. Li, M. Gao, Y. Gu, L. Li, Y. Liu, H. Lin, X. Zhang, B. Zhao, T. Liu, Y. Yang, Z. Li, X. Zhou, X. Gao, Introduction of the X-ray diffraction beamline of SSRF, Nucl. Sci. Tech. 26 (2015) 020101, https://doi.org/10.13538/j.1001-8042/nst.26.020101

[21] M. Jia, K. Zhai, M. Gao, W. Wen, Y. Liu, X. Wu, S. Zhai, Raman spectra and X-ray diffraction of merrillite at various temperatures, Vib. Spectrosc. 106 (2020) 103005, https://doi.org/10.1016/j.vibspec.2019.103005

[22] W. Xue, K. Zhai, S. Zhai, Thermal expansion of ellinaite (β-$CaCr_2O_4$): An in-situ high temperature X-ray diffraction study, Phys. Chem. Miner. 48 (2021) 2, https://doi.org/10.1007/s00269-020-01126-2

[23] B.H. Toby, EXPGUI, a graphical user interface for GSAS, J. Appl. Crystallogr. 34 (2001) 210–213, https://doi.org/10.1107/S0021889801002242

[24] A.C. Larson, R.B. Von Dreele, General structure analysis system (GSAS), Los Alamos Natl. Lab. Rep. LAUR (2004) 86–748.

[25] L. Zhang, S. Yan, S. Jiang, K. Yang, H. Wang, S. He, D. Liang, L. Zhang, Y. He, X. Lan, C. Mao, J. Wang, H. Jiang, Y. Zheng, Z. Dong, L. Zeng, A. Li, Hard X-ray microfocusing beamline at SSRF, Nucl. Sci. Tech. 26 (2015) 060101, https://doi.org/10.13538/j.1001-8042/nst.26.060101

[26] Z. Li, Y. Yin, J.D. Rumney, S.R. Shieh, J. Xu, D. Fan, W. Liang, S. Yan, S. Zhai, High-pressure in-situ X-ray diffraction and Raman spectroscopy of Ca_2AlFeO_5 brownmillerite, High. Press. Res. 39 (2019) 92–105, https://doi.org/10.1080/08957959.2019.1571587

[27] M. Jia, X. Hu, Y. Liu, S. Jiang, X. Wu, S. Zhai, X-ray diffraction and Raman spectra of merrillite at high pressures, High. Press. Res. 40 (2020) 411–422, https://doi.org/10.1080/08957959.2020.1798945

[28] H.K. Mao, J. Xu, P.M. Bell, Calibration of the ruby pressure gauge to 800 kbar under quasi-hydrostatic conditions, J. Geophys. Res. 91 (1986) 4673–4676, https://doi.org/10.1029/JB091iB05p04673

[29] C. Prescher, V.B. Prakapenka, DIOPTAS: a program for reduction of two-dimensional X-ray diffraction data and data exploration, High. Press. Res. 35 (2015) 223–230, https://doi.org/10.1080/08957959.2015.1059835

[30] Y. Fei, Thermal expansion, in: T.J. Ahrens (Ed.), Mineral Physics & Crystallography: a Handbook of Physical Constants, American Geophysical Union, Washington DC, 1995, pp. 29–44, https://doi.org/10.1029/RF002p0029

[31] K. Kurosaki, T. Tanaka, T. Maekawa, S. Yamanaka, Thermal properties of polycrystalline sintered SrY_2O_4, J. Alloy. Compd. 395 (2005) 318–321, https://doi.org/10.1016/j.jallcom.2004.11.041

[32] R.M. Hazen, C.T. Prewitt, Effects of temperature and pressure on interatomic distances in oxygen-based minerals, Am. Mineral. 62 (1977) 309–315, https://doi.org/10.1029/SP026p0407

[33] F. Birch, Finite elastic strain of cubic crystals, Phys. Rev. 71 (1947) 809–824, https://doi.org/10.1103/PhysRev.71.809

[34] R.J. Angel, Equations of state, Rev. Miner. Geochem. 41 (2000) 35–59, https://doi.org/10.2138/rmg.2000.41.2

[35] The Materials Project, ⟨https://materialsproject.org/materials/mp-4056/⟩.

[36] D.L. Anderson, O.L. Anderson, The bulk modulus-volume relationship for oxides, J. Geophys. Res. 75 (1970) 3494–3500, https://doi.org/10.1029/JB075i017p03494

[37] J. Philippen, Fiber crystal growth of cerium dopedcalcium scandate, strontium yttrium oxide, and tristrontium silicate,PhD thesis, Technical University of Berlin, 2013.

[38] C. Guguschev, J. Philippen, D.J. Kok, T. Markurt, D. Klimm, K. Hinrichs, R. Uecker, R. Bertram, M. Bickermann, Czochralski growth and characterization of cerium doped calcium scandate, CrystEngComm 19 (2017) 2553–2560, https://doi.org/10.1039/C7CE00445A

[39] S.W. Kieffer, Thermodynamics and lattice vibrations of minerals, 1. Mineral heat capacities and their relationships to simple lattice vibrational models, Rev. Geophys. Space Phys. 17 (1979) 1–19, https://doi.org/10.1029/RG017i001p00001

[40] S.W. Kieffer, Thermodynamics and lattice vibrations of minerals, 3. Lattice dynamics and an approximation for minerals with application to simple substances and framework silicates, Rev, Rev. Geophys. Space Phys. 17 (1979) 35–59, https://doi.org/10.1029/RG017i001p00035

[41] S.W. Kieffer, Thermodynamics and lattice vibrations of minerals, 4. Application to chain and sheet silicates and orthosilicates, Rev, Geophys. Space Phys. 18 (1980) 862–886, https://doi.org/10.1029/RG018i004p00862

[42] E. Kroumova, M.I. Aroyo, J.M. Perez-Mato, A. Kirov, C. Capillas, S. Ivantchev, H. Wondratschek, Bilbao crystallographic server: useful databases and tools for phase-transition studies, Phase Transit. 76 (2003) 155–170, https://doi.org/10.1080/0141159031000076110

[43] F. Birch, The velocity of compressional waves in rocks to 10 kilobars, Part 2, J. Geophys. Res. 66 (1961) 2199–2224, https://doi.org/10.1029/SP026p0091

[44] Y. Sueda, T. Irifune, T. Sanehira, T. Yagi, N. Nishiyama, T. Kikegawa, K. Funakoshi, Thermal equation of state of $CaFe_2O_4$-type $MgAl_2O_4$, Phys. Earth Planet. Int. 174 (2009) 78–85, https://doi.org/10.1016/j.pepi.2008.07.046

[45] X. Luo, B. Wang, Structural and elastic properties of $LaAlO_3$ from first-principles calculations, J. Appl. Phys. 104 (2008) 073518, https://doi.org/10.1063/1.2990068

[46] O.L. Anderson, A simplified method for calculating the Debye temperature from elastic constants, J. Phys. Chem. Solids 24 (1963) 909–917, https://doi.org/10.1016/0022-3697(63)90067-2